High Pressure in Boron Nitride Nanotubes for Kirigami Nanoribbon Elaboration

Silvio Silva-Santos, Anthony Impellizzeri, Acrisio Aguiar, Catherine Journet, Charline Dalverny, Bérangère Toury, José de Sousa, Chris Ewels, Alfonso San-Miguel

High Pressure in Boron Nitride Nanotubes for Kirigami Nanoribbon Elaboration

S.D. Silva-Santos,[†,#] A. Impellizzeri,[‡] A.L. Aguiar,[¶] C. Journet,[§] C. Dalverny,[‖] B. Toury,[§] J.M. De Sousa,[⊥] C.P. Ewels,[‡] and A. San-Miguel[*,†]

†*Université de Lyon, F-69000 Lyon, France and Institut Lumière Matière, CNRS, UMR 5306, Université Lyon 1, F-69622 Villeurbanne, France*

‡*Institute des Matériaux Jean Rouxel (IMN), CNRS UMR6502/Université de Nantes, Nantes 44322, France"*

¶*Departamento de Física, Universidade Federal do Piauí, Teresina, Piauí, 64049-550, Brazil*

§*Université de Lyon, F-69000 Lyon, France and Laboratoire Multimatériaux et Interfaces, CNRS, UMR 5615, Université Lyon 1, F-69622 Villeurbanne, France*

‖*Université de Lyon 1, F-69000 Lyon, Centre Technologique des Microstructures, 5 rue Raphael Dubois, 69622 Villeurbanne Cedex, France*

⊥*Instituto Federal do Piauí - IFPI, São Raimundo Nonato, Piauí, 64770-000, Brazil*

#*Current address: Electrical Engineering Department, Laboratory of Nanoelectronics and Nanophotonics, Federal University of Pará, PO Box 8619, Agencia UFPA, CEP 66075-900 Belém, Pará, Brazil*

E-mail: alfonso.san-miguel@univ-lyon1.fr

Abstract

Cutting and folding 2D systems is one of the explored paths to tune physical and chemical properties in atomic thick matter. Contrarily to graphene, boron nitride

(BN) nanoribbons are difficult to obtain and their folded structures have not been yet reported. Here we show that pressure application in multiwall boron nitride nanotubes leads to different types of tube internal organizations including BN nanoribbon formation and folds. The new observed tube-structures are associated to the breaking of a number of the internal tubes leading either to non-organized structures in the form of internal tube alveoli or in an organized stacking of folded h-BN nanoribbons. Irreversible changes in the morphology of multiwall BN nanotubes (MWBNNTs) take place from ∼7 GPa and morphologically modified tubes could be observed up to pressures of at least 49 GPa. The here used experimental probes included high resolution transmission microscopy, electron tomography and Raman spectroscopy. Atomistic modelling was also performed showing the formation of pinch structures along the tubes which favour pressure induced bond-breaking and hybridization changes and confirming the folded structure. Both experiments and modelling show that tube polygonization is a prominent characteristic of MWBNNTs even at ambient pressure. Overall, the pressure evolution of MWBNNTs strongly differs from their carbon analogues. The high mechanical stability of BN tube geometry is of interest for composite based structural materials. On the other side, the availability of h-BN nanoribbons and folded structures opens new prospects to produce physically modified BN properties.

Keywords

Boron Nitride Nanotubes, High Pressure Raman Spectroscopy, Electronic Microscopy, Electronic Tomography, Nanomechanics, Phase Transitions (Kirigami)

Introduction

Origami and Kirigami are the Japanese traditional artistic techniques allowing to modify a paper shape either by folding (Origami) or by combining folds and cuts (Kirigami). These traditional methods are becoming increasingly inspiring in nanotechnology [1,2] as novel means

to elaborate 3D mesostructures[3,4] or for dynamically adjust the physico-chemical properties in nanostructures[5] including electrical resistance,[6] surface physical properties[7] or biotechnology.[8] Pressure application is one particular approach to fold and cut nanosystems[9] which has been successfully used to generate the stochastic corrugation of 2D systems as graphene[10,11] or MoS_2.[12]

Nanotubes unzipping (cut) or their radial deformation (fold) can also be reached through high pressure application and it has extensively studied in carbon nanotubes. In fact, under high pressure, the radial cross-section of carbon nanotubes evolves through different geometries including its collapsed form and this has been shown both theoretically[13–15] and experimentally.[16–21] Pressure induced unzipping of carbon nanotubes has been also demonstrated experimentally.[22,23]

In the case of boron nitride nanotubes (BNNTs), the presence of a pressure induced radial collapse has been predicted through different atomistic modelling approaches[24–26] but no experimental confirmation has been reported. The situation is even less clear concerning tube unzipping for which there are no reports showing the existence of a high pressure route. Nevertheless, it has been shown that sonication[27] or acid treatment[28] can be partially successful in BNNTs unzipping.

We will present here pressure induced kirigami structures (combinations of cuts and folds) obtained through the high pressure treatment of BNNTs leading in particular to nanoribbon formation. Moreover we will show that other pressure induced structural modifications of BNNTs can be obtained and we will idiscuss the general pressure evolution of multi-walled boron nitride nanotubes (MWBNNTs) and its differences with respect to MWCNTs. Our study includes the *in situ* study of samples using Raman spectroscopy, high-resolution transmission electron microscopy (TEM) and TEM tomography on recovered samples as well as molecular dynamics (MD) and density functional theory (DFT) modelling.

BNNTs were initially predicted by computational simulation in 1994[29,30] and synthesized by the arc-discharge method in 1995.[31] Compared to CNTs, which can be metallic or semi-

conducting depending on chirality, BNNTs have a large band gap beyond 5 eV [32] (insulating nature) with weak dependence on chirality. [29,30,32,33] BNNTs exhibit high chemical stability, [34] thermal stability and conductivity [35,36] and a high Young's modulus value. [37,38] These properties are sometimes complementary to those of CNTs and make BNNTs promising candidates for advanced material technologies, such as in the development of photoluminescence or optoelectronic devices or piezoelectric materials, [38,39] drug delivery systems [40] or in biological applications [41] as for instance in nanotech-assisted tissue-engineered platforms for muscle stimulation. [42] However, their development and production for practical applications still depend on trustworthy synthesis methods, analytical characterizations, together with an improved knowledge of the structure-property relationships.

The characterization of mechanical properties of nanotubes constitutes an important subject in view of applications. [9,43] In particular, the effective radial elastic modulus of SWBNNTs (single wall boron nitride nanotubes) is smaller than for SWCNTs [44] (single wall carbon nanotubes), and - as in CNTs - it increases rapidly with the number of walls. [45] The high pressure evolution of carbon nanotubes is characterized by its radial collapse, i.e., the transition towards a flattened tube. In particular theoretical and Raman experimental works agree that the radial collapse pressure, P_c, of single-wall CNTs strongly depends on the tube diameter, following a modified Lévy-Carrier law $P_c d^3 = \alpha\,(1 - \beta^2/d^2)$ (d tube diameter or the internal diameter in few-wall tubes and α and β physically significant coefficients). [12,15,21,46,47]

The formation of graphene nano-ribbons beyond the radial collapse of carbon nanotubes has been reported for the high pressure and high temperature shock-wave transformation of double-wall carbon nanotubes [48] and in the high pressure transformation of triple-walled carbon nanotubes. [23] Up to now, there is no experimental evidence of a similar behavior in BNNTs.

All high pressure experiments on BNNTs concern MWBNNTs. Saha et al. [49,50] explored the high pressure behavior of MWBNNTs by Raman spectroscopy up to 12 GPa where they lost irreversibly the Raman signal. This was interpreted as an amorphization of the

structure. In a subsequent high pressure synchrotron X-ray diffraction study of MWBNNTs up to 19.1 GPa,[51] it was shown that MWBNNTs remained crystalline up to that maximum pressure. In that work it was observed the irreversible appearance of new diffraction peaks from 3.2 GPa which were assigned to the wurtzite-BN phase. On the other side, Dong et al.[52] carried out *in situ* IR measurements at high pressure also in MWBNNTs up to 35 GPa. Comparing MWBNNTs with bulk h-BN it was observed that both samples undergo at $\sim$ 11 GPa a transformation towards the formation of sp^3 bonding, associated with the w-BN metastable phase.[53] At $\sim$ 23 GPa the transition is almost complete for bulk h-BN, whereas for MWBNNTs even at $\sim$ 35 GPa the transformation is far from complete. A two-step transformation mechanism for sp^3 bonding formation in MWBNNTs was proposed: first inter-tubular connections in bundles are formed around 11 GPa and secondly intra-tubular connections were considered to become significant above 20 GPa. Under decompression only the intra-tubular connexions remain.

To summarize, whereas theoretical works in BNNTs focus in the observation of pressure induced radial collapse transitions similarly to the known scheme in CNTs, none of the experiments performed up to now provide evidence of such transition. In CNTs it is not easy to provide experimental evidence on the radial collapse high pressure transformation of MWCNT, but it has been nevertheless recently provided in composite systems[54] and in triple-wall carbon nanotubes.[23] Such difficulty may also apply to BNNTs, for which all experiments concern also the multi-wall case. Evidence of a structural evolution of MWBNNTs which includes the formation either of sp^3 bonding or even the transformation towards w-BN is pointed out by experiments, but without consensus on the pressure at which the transformation takes place and its detailed nature.

Our work is then motivated by the need of experimental and theoretical studies to clarify the high pressure structural evolution of MWBNNTs and to establish if a parallel with the high pressure evolution in CNTs is pertinent in particular concerning modifications on the geometry leading to folds and cuts.

Results

Transmission Electron Microscopy Analysis

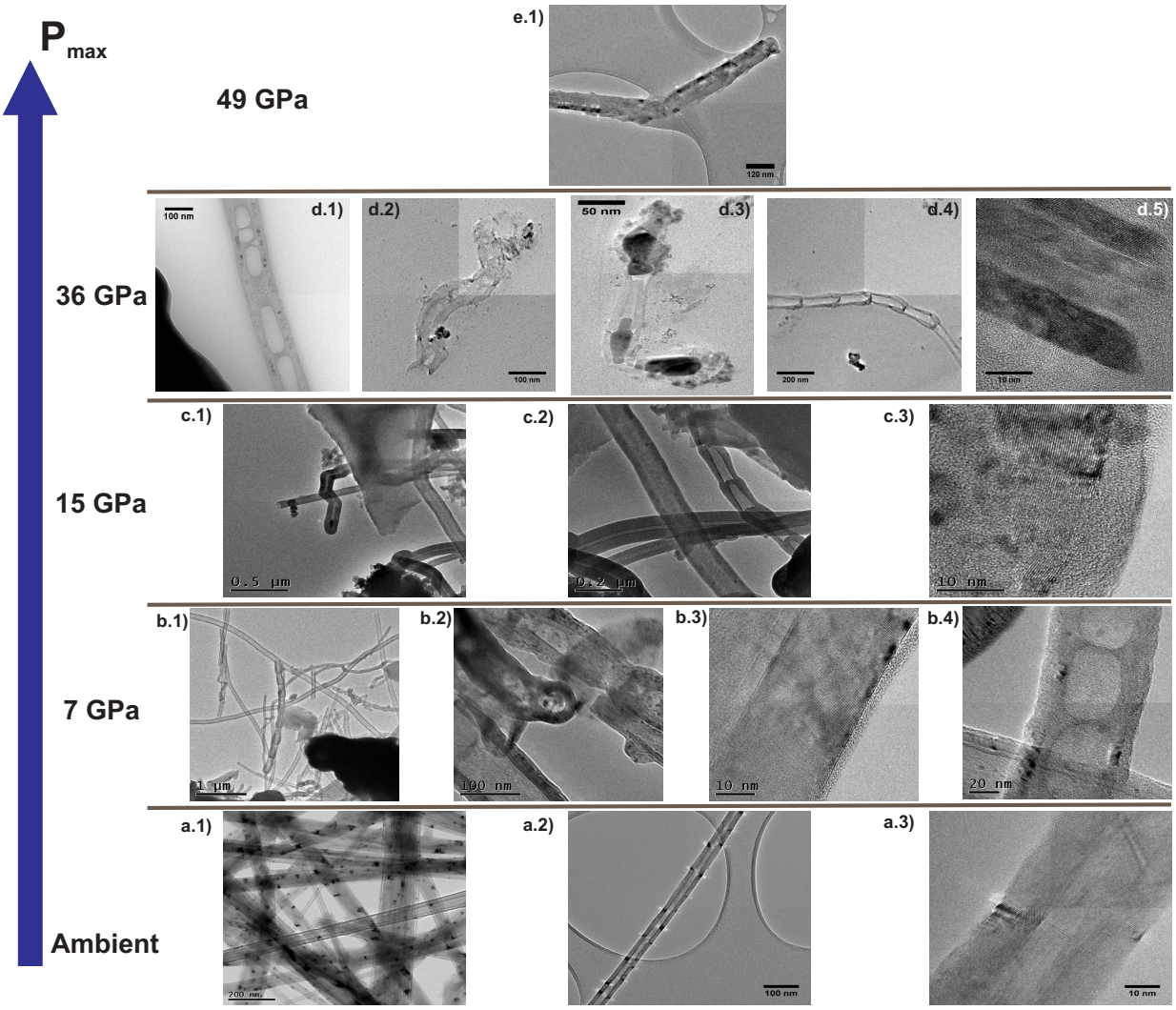

Figure 1: HRTEM images of the pristine MWBNNTs sample (ambient) and after pressure cycles up to 7, 15, 36 and 49 GPa. Scales are provided in each image.

In order to obtain a better insight on the pressure evolution of MWBNNTs we have compared TEM images of pristine and recovered samples cycled up to pressures of 7, 15, 36 and 49 GPa. The most significant images are shown in Fig. 1 where we can appreciate important changes in the tube morphology. At ambient conditions the MWBNNTs showed dark (or bright) spots along the tube axis which are well evident in panels a.1 to a.3 in

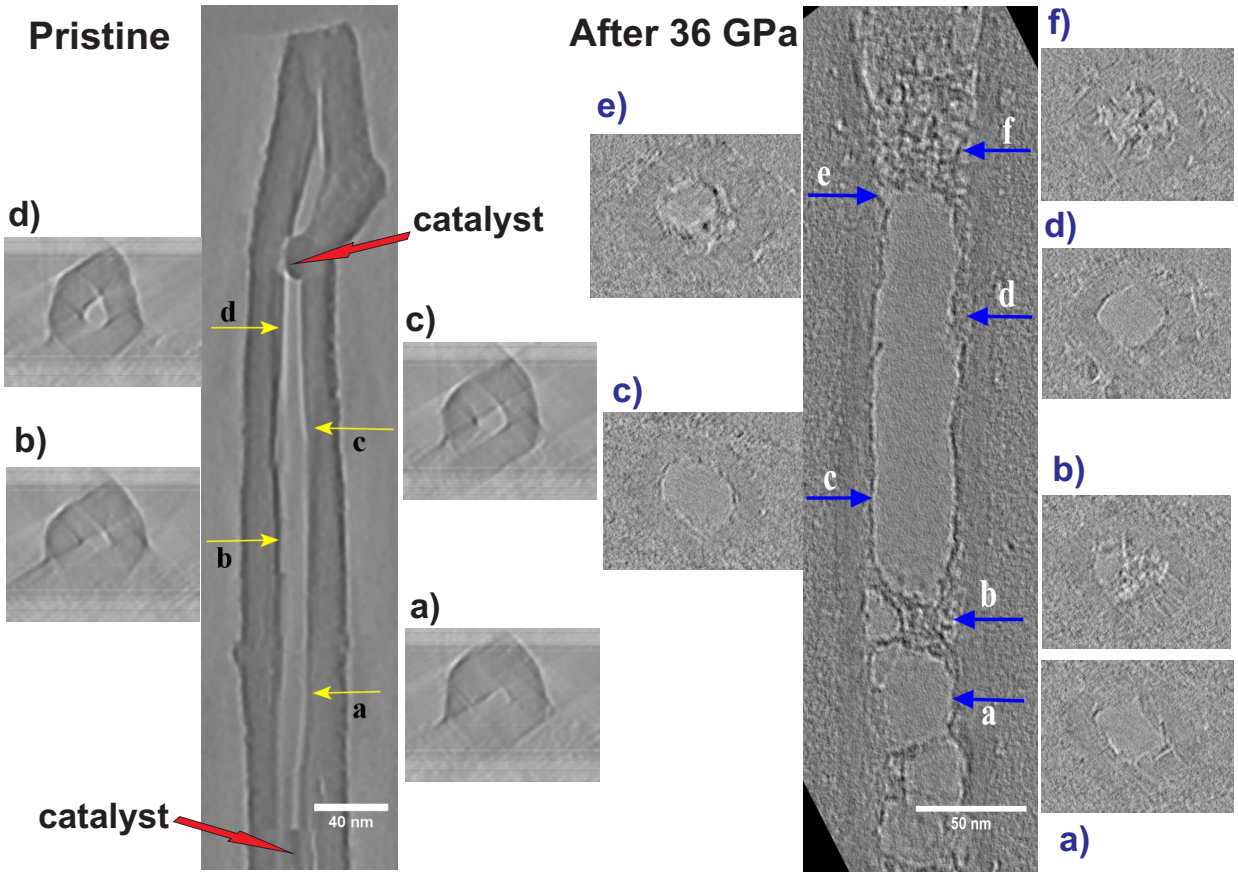

Figure 2: HRTEM Tomography images of a pristine MWBNNT (left) and of another tube after a pressure cycle of 36 GPa (right). The arrows show perpendicular cross sections along the tube labelled a) to d) for the pristine tube and a) to f) for the pressure cycled tube. The internal "diameter" of the tube in the non-closed regions evolves typically from 15 to 20 nm for the pristine tube (in the region between a and d) and between 36 and 40 nm (in the region between c and d) for the cycled tube. The average value of the external tube diameter is 52 and 66 nm for the pristine and the cycled tube respectively.

Fig. 1. This regular pattern has been associated to the helical polygonization of internal tubes[55,56] and non-regularities in the spotty pattern have been attributed to local internal polygonization.[57] Some works point out also to polygonization of the external tubes for large tube diameteres.[58] We may note that after pressure cycling, even at the lowest pressures of 7 GPa, such regular spotty patterns were not observed and only local dark regions could be observed in some tubes. Images from the samples recovered after 7 GPa of pressure, preserved the tube geometry as can be seen in Fig. 1 b.1. We nevertheless observed the presence of tubes presenting bamboo-like structure which we never observed in pristine samples (Fig. 1

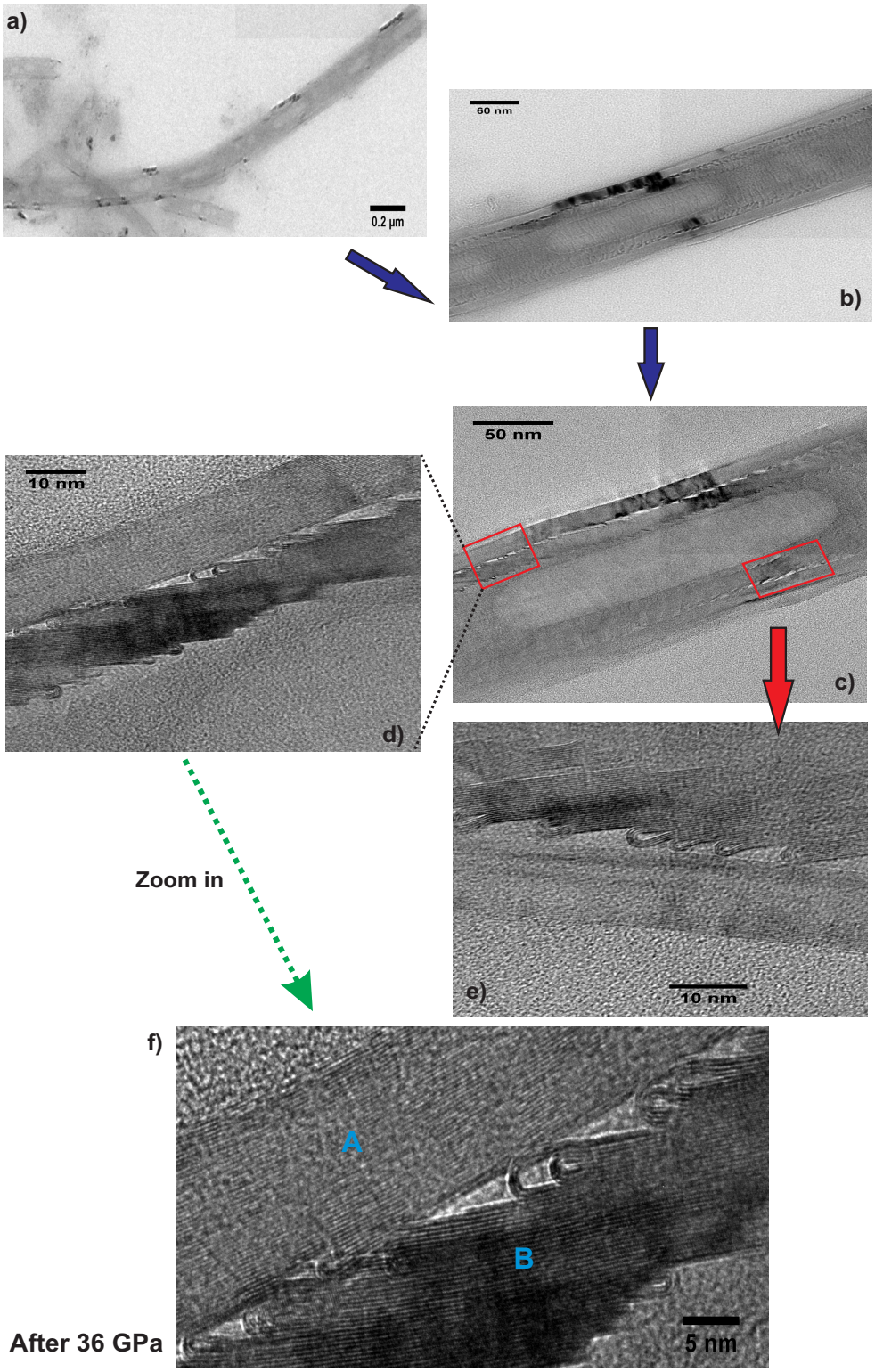

Figure 3: HRTEM images of a particularly interesting pressure modified MWBNNT after a pressure cycle up to 36 GPa. a) Image of the several microns length tube showing various internal alveoli of irregular size and spacing. b) to e) detail of the structure at different scales in which a very particular structure made of BN folded nanoribbons is observed. The two distinct more external regions are shown in f) and labelled A and B.

b.1). In addition, in certain regions the tubes showed a deformation along the tube (Fig. 1 b.2) which can be interpreted associated to a radial cross section modulation. Furthermore a local densification on the tube walls was also observed in some tubes as can be seen in Fig. 1 b.3 and which can be associated to local tube flattening of all or part of the tube walls.[57] All changes observed in the 7 GPa sample become more pronounced for the tubes recovered after 15 GPa (Fig. 1 c.1 to c.3). The sample recovered from a pressure cycle up to 36 GPa showed much more significant transformations (Fig. 1 panels d.1 to d.5). Most tubes were extremely damaged as can be seen in Fig. 1 d.2 and d.3. Nevertheless it was possible to observe some bamboo-like tubes (Fig. 1 d.4), alveolar-tube structures (Fig. 1.d.1) and some zones presenting high densification as shown in Fig. 1 d.5. After a pressure cycle at the highest attained pressure of 49 GPa, it was still possible to observe tube-like structures as the one shown in Fig. 1.e.1. There is nevertheless few evidence of empty or low-density internal zones, and the structure looks very inhomogeneous and disorganized.

3D TEM tomography images were obtained for a MWBNNT at ambient pressure and for another tube recovered after a pressure cycle up to 36 GPa. The obtained views along the tube axis and cross-sections at different positions are shown in Fig. 2 (see also S.I. for tomography video images). We can observe that in both cases the external and internal cross-sections morphologies evolve along the tube. The pristine tube showed the presence of encapsulated catalyst particles and multiple faceted rhombus polygonal internal cross-section with a modulated size and an external cross-section varying from hexagonal to rhombus. As already discussed, polygonal cross-sections for all or part of MWBNNTs has been reported in a number works.[55–57,59,60] We should note that most observed polygonal cross-section in previous works are hexagonal but rhombic cross sections have been also observed[60]). Rhombus cross-sections were also observed in the tube recovered from 36 GPa in which other morphologies (ovalized or highly deformed) were also present. We also notice the complexity of the internal structure of the recovered nanotube showing some highly disordered closed or bridged parts in the internal cross-section.

A very unique structure with a new type morphology was observed after a pressure cycle up to 36 GPa. In Figure 3 are shown different TEM views at various scales of this novel tube morphology. First we note that the tube presents a kind of irregular inner alveolar structure which reminds the recovered tube after pressure cycle in Fig. 2 or the ones in Fig. 1 b.4 or d.1. More interestingly, we note that the tube wall is now divided in two regions (in Fig. 3.f). The external region (region A) is a multi-walled tubular structure made of about 40-50 tubes with an external diameter of about 110-120 nm and a thickness of about 15 nm. The inter-tube distance is of 0.35 nm. The internal region (region B) can be described as a domino stacking of one-closed-edge boron-nitride nanoribbons, i.e., folded nanoribbons, stacked in two sides of the tube and exhibiting close to a mirror symmetry with respect to the nanotube axis. The length occupied by the folded nanoribbons on each side of the tube represents approximately 1/6 of the length of the tubes which would have occupied the same space. The closed lobes have different hierarchical structures as can be appreciated in Fig. 3.d and Fig. 3.e. The lobe terminations are observed both in the internal and in the external sides and can be seen as multi-folded boron-nitride nanoribbons. In Fig. 3.d can be appreciated that there are some connection points between region A and region B, whereas in Fig. 3.e the two regions are well dissociated. The nano-ribbons form an angle of $\sim 15^\circ$ with respect to the tube axis running all along the tube without interruption. This inclined structuration can be related to the spiral-type structure of polygonized BNNTs[55,61] and, as it will be discussed later, may arise through a pressure induced kirigami process.

Raman Spectroscopy

High pressure Raman spectroscopy in BNNTs suffers from limitations associated with sample purity, fluorescent BNNTs background and the proximity between the main Raman tangential mode (E_{2g}) of BNNTs (1360 cm^{-1}) and the prominent diamond Raman mode (1332 cm^{-1})[62] arising from the use of diamond anvil cell pressure apparatus. Nevertheless it remains a practical technique to explore the high pressure properties on BNNTs in particular

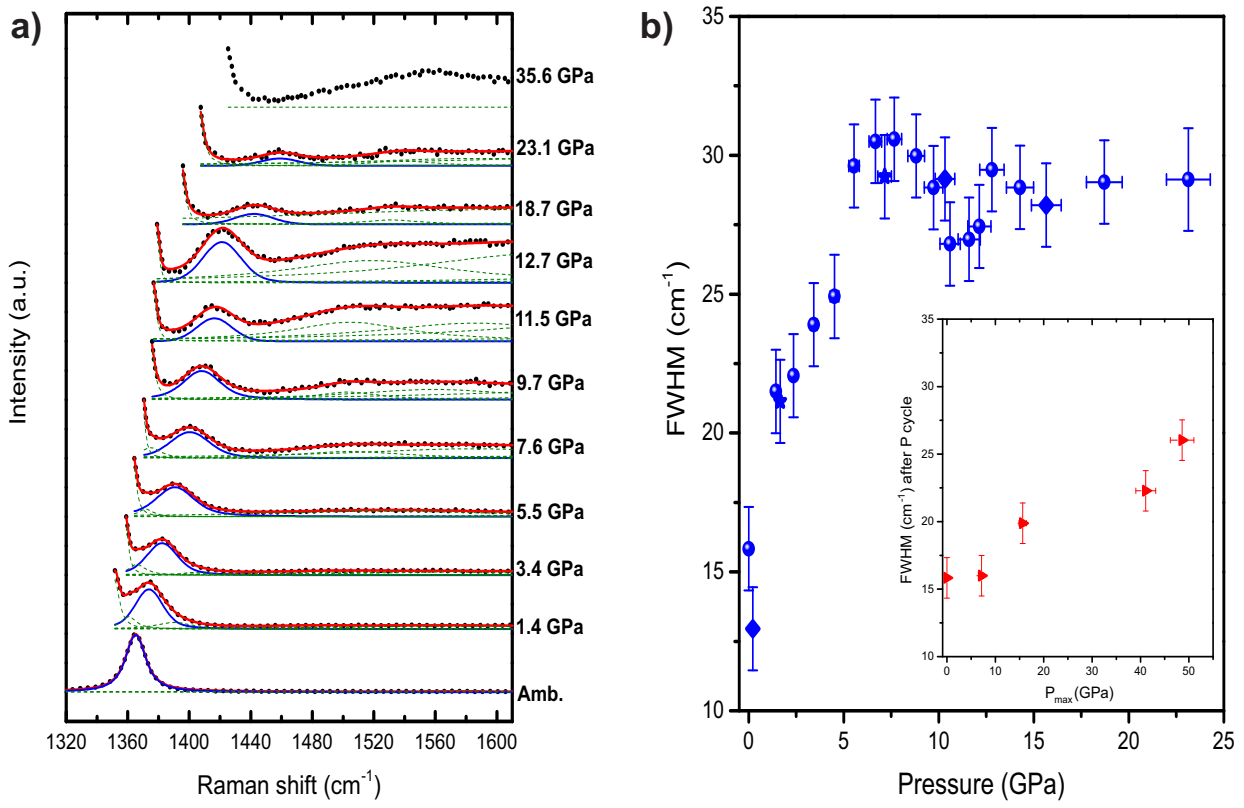

Figure 4: (a)*In situ* Raman spectra of MWBNNTs during a compression run up to 36 GPa (black dots). Continuous lines (in red) superposed to dots (experimental data) are the fitted function obtained by considering Voigt curves. The MWBNNTs tangential modes (blue continuous line) and the background and diamond anvil contributions (green dashed lines) are also shown. (b) Corresponding *in situ* FWHM evolution. The inset shows the obtained *ex situ* FWHM as function of the reached maximum pressure.

thanks to the parallel which can be made with the high pressure study of CNTs. Up to now there is no evidence of an spectral signature which could be related to BNNTs collapse as it has been found for CNTs.[63]

We show in Fig.4.a the Raman spectra of the E_{2g} tangential mode (TM) for the compression experiment from ambient pressure (outside of the pressure device) up to 36 GPa. This peak blue-shifts gradually up to $\sim$ 23 GPa, where it becomes very weak and cannot be further detected. The highest pressure spectrum at $\sim$ 36 GPa shows just the presence of a broad background signal. The TM signal was fitted using a Voigt profile including a background signal due to fluorescence (dashed lines). The intensity rise at the low energy side of the spectra is due to the diamond Raman peak contribution from the pressure cell diamond

anvils. We may note that differences in intensity between the spectra are not significant due to the lack of a normalization signal.

As it is shown in Fig. S2.a of the Supplementary Information, the evolution of E_{2g} mode energy is linear up to the maximum pressure detected of 24 GPa with a slope of $\partial\omega_{E_{2g}}/\partial P = 4.02\ cm^{-1}/$ GPa and ambient pressure intercept frequency at $1368\pm 1\ cm^{-1}$ in good agreement with the TM frequency of $1365 \pm 2\ cm^{-1}$ measured outside of the cell. The obtained pressure slope for the E_{2g} is in good agreement with the values obtained in a previous works.[49,50] Nevertheless we note that in the work of Saha et al[49] deviations from linearity were observed from 10 GPa and the TM signal was lost at 12 GPa, i.e., at a pressure two times smaller than in our measurements. In Fig.4.b it is shown the corresponding pressure evolution of the Full Width at Half Maximum (FWHM) of the E_{2g} mode. The E_{2g} first enlarges rapidly up to around 8 GPa from where an abrupt decrease is observed. This dip in the pressure evolution is followed by a plateau region for pressures beyond 12 GPa. The ambient pressure value of the FWHM in our sample ($13\ cm^{-1}$) is significantly higher than in the case of Ref.[49] ($\sim 9\ cm^{-1}$). This is also the case for the pressure evolution of the FWHM which in the case of Ref.[49] it evolves linearly up to 10 GPa with a maximum value of $\sim 14\ cm^{-1}$ which is about half of our values for the same pressures. Differences in the sample's crystallinity and in the hydrostaticity of the used PTM can be at the origin of such observations.

Raman spectra could be recorded for the recovered samples after pressure cycles up to 7.1, 15.6, 41.1 and 48.6 GPa and compared with the pristine sample (Fig S2.b of S.I.). Within error bars there is no change in the E_{2g} position of the TM mode after all pressure cycles. Nevertheless some modifications can be noticed comparing the different spectra. The spectra from pressure cycles up to 41.1 GPa and 48.6 GPa show the presence of a new broad band at $\sim 1280\ cm^1$. The same peak but much weaker can be already observed for the sample having been cycled up to 15 GPa but it is absent for the lower pressure points. In the inset of Fig.4.b it is shown the evolution of E_{2g} FWHM for the recovered MWBNNTs as function

of the maximum reached pressure. It is observed that the two first spectra (ambient and 7 GPa of cycling pressure) have a FWHM $\sim 16\ cm^{-1}$ while after cycling at higher pressure the E_{2g} broadens significantly concomitantly to the appearance of the new above referred peak. All these Raman results point then to a regime of irreversible changes taking place from 11 $\pm$ 4 GPa. Coupled to the previous TEM observations, it appears that the lower limit of 7 GPa, needs to be considered.

HRTEM, Raman and 3D tomography experiments point out to a richer high pressure phase diagram in MWBNNTs than in MWCNTs.[47] We have then performed on one hand MD simulations to try to better understand the high pressure transformation mechanisms in MWBNNTS and on the other side DFT modelling in order to better understand the particular folded structure observed at 36 GPa. The following sections present that results.

Reactive Molecular Dynamic Simulations

The experimentally studied BNNTs in our work have outer diameters of the order of various tenths of nm and are made by the concentric stacking of several tenths of tubes as observed in TEM images (Fig. 1). Roughly, by using an atomistic modelling, we can estimate that such BNNTs nanotubes are composed of 25 concentric walls (thickness of 10 nm) and at least of 450 zigzag-type unit cells for describe the exotic pressure-induced formations (bamboo-like structure seems to be at least 200 nm long). This MWBNNT should have close to 10 billions of atoms, a number which is prohibitive from computational point of view, even using a potential models in molecular dynamics (MD) framework. Modelling the physical properties of a reasonable multi-layered tube length of such characteristics is challenging, specially under extreme high-pressure conditions. For that reasons we have made the choice to use MD simulations to study the effect of the internal diameter and/or the effect of the number of layers on the structure of few-layer BNNTs at ambient conditions. After that, we have considered the effect of pressure on a bundle of 3-wall BNNTs. Even if a direct

comparison with experiments is then not possible, we will examine the common trends or analogies which may emerge. In special, we are interested in analyzing the pressure effect on the innermost tubes which seems to experience, as observed previously in the experiments, strong modifications due to the high-pressure conditions. More details on the modelling methodology are provided in S.I.

Thermalization: ambient pressure polygonal structures

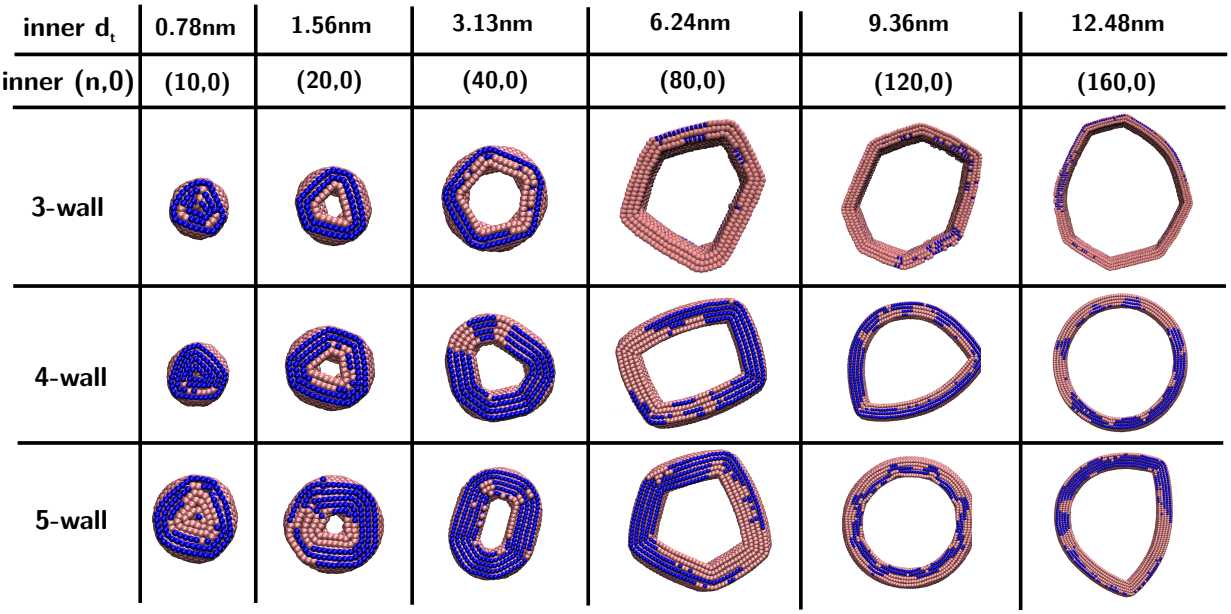

Figure 5: Fully relaxed structures of 18 3-walled (1st line), 4-walled (2nd line) and 5-walled MWBNNTs (5th line) after 200ps at 300K.Structures in the same column have the same internal diameter. Both the chiral indexes and the diameter of the internal tube are given for each column.

We first performed structural thermalization of several 3-walled, 4-walled and 5-walled MWBNNTs. Tube cross-sections of the final relaxed structures are shown in Fig.5. We note that almost all MWBNNTs studied present polygonized or flattened walls. In such calculations we considered the diameter of the innermost tube d_{in} as a characteristic geometrical parameter. This consideration is based on the pressure evolution of double and triple walled CNTs which is mainly dependent on the innermost tube diameter.[12] Even for

small diameters (∼0.78nm) 3-walled MWBNNT, the innermost tube is found to be polygonized. Surprisingly, large-diameter 4-wall and 5-wall MWBNNTs were found to have not flattened surface and even at some cases, perfectly circular MWBNNTs were observed. Golberg et al.[34] have proposed perfectly circular outer walls (large diameter) and faceted inner walls (small diameters) of MWBNNTs to explain the observed spotty patterns of HRTEM. Therefore, our calculations also supports those experimental observations. This could also indicate that length/diameter (L/dt_{in}) aspect ratio is an important factor to observe flattening of MWBNNT during room-temperature thermalization, since we use a very small L/dt_{in} ratio (1.70nm/9.36nm). Even if thermal calculations are performed using periodic conditions in z-axis direction, the supercell used here is small when compared to MWBNNT diameter range which could increase some surface energetic barriers which promotes the modulated flattening observed on the small diameter MWBNNTs of Fig.5.

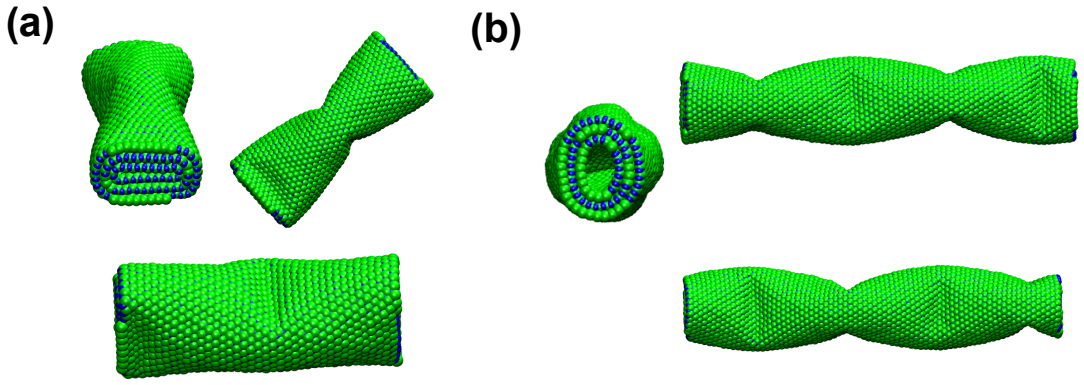

Figure 6: Fully relaxed structures of two 3-walled MWBNNTs after 200ps at 300K. (a) Snapshots of the thermalized structure of the (20,0)@(28,0)@(36,0) MWBNNT with with 20 units cells (∼8.52nm). (b) The thermalized structure of the (20,0)@(28,0)@(36,0) MWBNNT with with 20 units cells (∼17.04nm).

In order to avoid L/dt_{in} aspect ratio effects, we also performed room-temperature thermalization of very long MWBNNTs. The 3-walled BNNT (20,0)@(28,0)@(36,0) was studied with 20 and 40 units cells. This provides respectively 3-walled BNNTs of 8.52nm and 17.04nm lengths. Fig.6.a displays the thermalized structure of the 20-unit cell (20,0)@(28,0)@(36,0) BNNT. It is interesting to note that cross-section faceting is no longer observed. However,

a modulated orthogonal collapse is observed even at ambient conditions. This modulated orthogonal collapse, which is similar to a local pinch, seems to be preserved even with the longer 3-walled BNNT, as can be observed in Fig.6b.

Bundle Compression: bond breaking and reconstruction

In order to observe the effect of such local pinches on high-pressure transformations of multi-walled BNNTs, we submitted the the 20-unit cell bundle (20,0)@(28,0)@(36,0) BNNT to high-compression conditions up to 107 GPa. We arranged such 3-walled BNNT in a triangular high-compacted bundle and we used the reduction of x-axis direction simulation box length for provide uniaxial compression on such bundle. The obtained results are shown in Fig. S3 of the S.I. and Fig. S4, where it is also shown the evolution of the number of BN bonds with pressure. It is interesting to note that BN bond breaking starts at around 30 GPa and becomes more significant after 60 GPa. After 102 GPa, there is clearly a faster breaking of nanotube structure which becomes irreversible after the pressure is released. However, as we can also observe in Fig. S3 (right panels), the overall bundle arrangement and the 3-walled BNNT structure is mainly preserved even if not all BN bonds are recovered. Very interestingly, Fig. S4 clearly shows that BN bond breaking is dominated by innermost tubes. A small amount of broken BN bonds comes from intermediate and outer tubes and together with innermost tube BN bonds are found to be irreversible.

From all those BN broken bonds we can also calculate the number of reconstructed bonds as a function of the pressure, which means that pressure creates a large amount of dangling bonds from boron and nitrogen dissociation. The increasing of confinement promotes bond reconstruction to form new B-N, B-B or N-N bonds in the same tube (intra-tube bonds) or between different walls of MWBNNT (intertube cross-linked bonds). Fig.S4 shows that bond reconstruction of innermost tubes starts at around 80GPa and becomes very relevant compared to the number of broken bonds. Those reconstructed bonds are also found to be irreversible. It should be stressed here that none intra-tube reconstructed bonds for

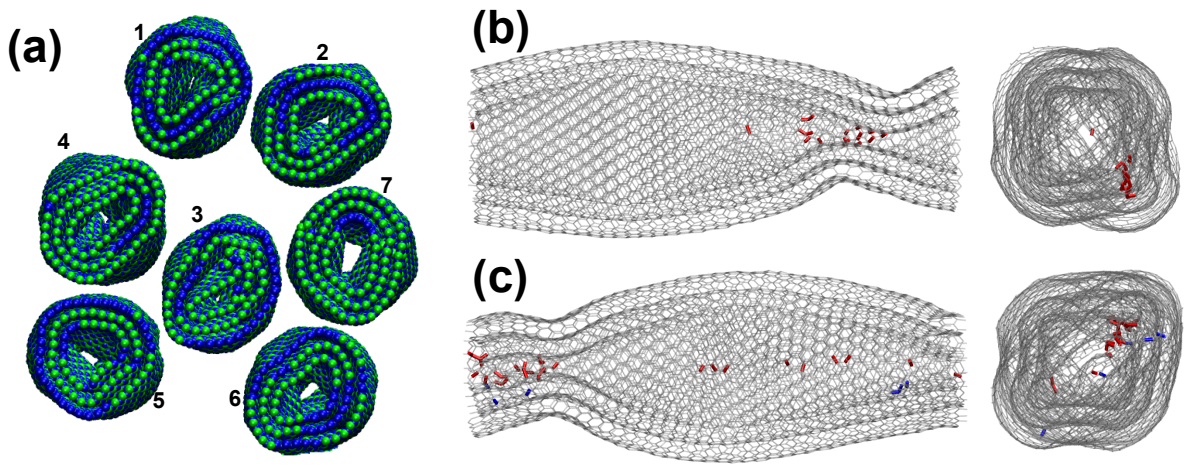

Figure 7: (a) Final structures of the (20,0)@(28,0)@(36,0) BNNT bundle after the decompression cycle (ambient pressure). Numbering is for tube identification. (b) Cross section and lateral view of tube labeled as 3. (c) Cross section and lateral view of tube labeled as 7. In (b) and (c) graphs, the BN unchanged bonds are in gray color and were made almost transparent for better visualization. Pressure-induced reconstructed bonds are highlighted in red (innermost) and blue (inter-tube) colours.

intermediate and outer tubes are observed, which evidences that innermost tubes of BNNTs are mainly affected by high pressure conditions. A very small amount of inter-tube bonds (between innermost-intermediate and outer-intermediate tubes) are also found and are not significant when compared to innermost bond breaking and reconstruction.

In Fig.7 it is shown the cross-section and lateral views of 3-walled BNNT bundles after the compression-decompression cycle. The individual tubes of the composite bundle were numbered for better identification. Tubes labeled with numbers 1,5 and 6 do not presented any bond reconstruction but only B-N bond breaking. Minor reconstructions (less than 5) were found in tubes numbers 2 and 4. Fig. 7.b, shows a colored graphical representation of tube labelled as "tube 3". Even if we can clearly see that the unbroken B-N bonds are dominant (grey color, transparent), a higher amount of intra-tube reconstructed bonds (red color, highlighted) can be visualized only for the innermost nanotubes. Fig. 7c, also shows a graphical representation of tube labelled as "tube 7". In this case, both inter-tube (blue color, highlighted) and intra-tube reconstructed bonds can be also visualized for the innermost nanotubes and we noted that intra-tube innermost reconstruction is again dominant.

Density Functional Calculations

In order to explore the pleated structures seen in the kirigami structures of Fig. 3.f, we performed a series of density functional theory (DFT) calculations (calculation details are given in methods section). Experimentally the folds show a continuous unbroken layer structure, each fold containing two to three layers. We simulate this here via a stacked series of collapsed double- walled BN nanotubes, a structurally equivalent system given the mechanical and electronic separation of the opposing folded sides. In order to determine the optimal nanotube pairing in this double-walled system, we first optimise different double-walled nanotube combinations (see Fig. 8). The most stable tube combinations are the (n,n) and (n+5,n+5), since a quite uniform interlayer spacing can be maintained around the cavities. This is therefore the combination we use in the following study.

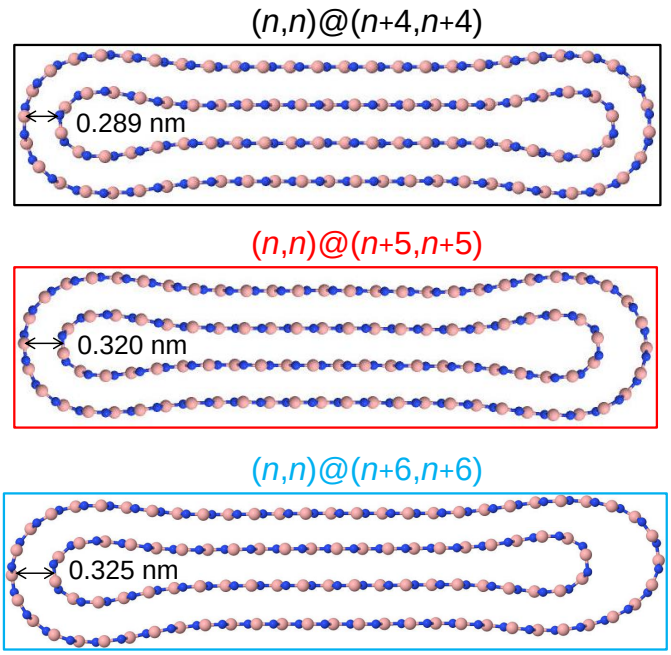

Figure 8: Density functional theory (DFT) relaxed cross-sections for different chirality combinations of armchair double-walled BN nanotubes. Interlayer spacings are marked in nm.

Pleating is a mechanism which allows contraction along the tube axis at the expense of radial expansion, suggesting that this structural motif is produced in response to axial rather than radial pressure, *i.e.* an interior cavity response to pressure applied at the open

tube ends. The pleating is observed only on the interior layers, and the external tube walls provide a physical diameter constraint which cannot be overcome without mass loss and restructuration. In this case the radial expansion can only occur through occupation of previously empty interior cavity volume, *i.e.* as the interior sections pleat and compress along the tube axis, they expand into the interior cavity space. In order to explore the relationship between compression and volume, we next optimised a 1D-infinite layer of collapsed double-walled BN nanotubes (see Figure 9). Each unit cell contains one collapsed double-wall tube (the infinite nanotube axis is defined as z, while the stacking direction is defined as x). The angle of inclination of the tube is determined by the width of the supercell along x, which we constrain in a sequence of calculations (Figure 9). The height we define as the difference in y between the highest and lowest B/N atoms in each case, with these x and y defining a collapsed nanotube area A in each case. We can see that as the x-value is decreased (corresponding to increasing pressure), the area A also decreases, suggesting a driving force under pressure to increase the buckle tilt angle. At the same time the infinite bilayer shows the lowest surface area which can be understood since the cavities are lower density than the bilayer region. Experimentally since the folds are much more spaced than in these simulations, this effect will be relatively smaller.

Table 1: DFT-D2 calculated width x (Å), height y (Å), and corresponding surface area A (Å^2) of 1D-row stacked double-walled collapsed BNNTs. x-values are fixed in each calculation. y values indicate height difference between minimum and maximum y coordinate of the B/N atoms, plus 3.35Å. Total energy values (in meV/atom) are given with respect to the "Vertical" configuration.

Configuration	x [Å]	y [Å]	A [Å^2]	E_{rel} [meV/atom]
Infinite bilayer	106.79	6.55	700	
Tilted (64°)	29.63	34.14	1012	9.26
Tilted (54°)	22.23	40.14	892	5.74
Tilted (44°)	17.87	46.05	823	2.11
Vertical (0°)	12.54	56.62	710	0.00

We next turn our attention to the folds at the edge of each pleat. Simulated HRTEM images are shown in Figure 10, which show good agreement with the experimentally observed

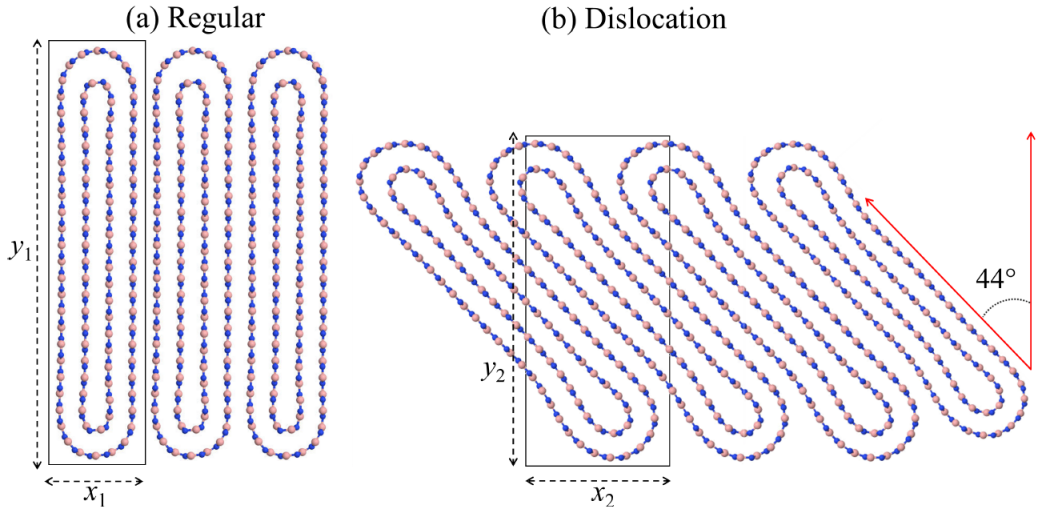

Figure 9: Density functional theory (DFT) relaxed cross-section for stacked 1D-row of collapsed double-walled BN nanotubes. Unit-cell width x (Å) is fixed in each case, y (Å) is marked with outline boxes, cell area A is marked beneath each image (Å^2), along with structure angle to the row (in degrees). (a) Vertical configuration (most stable) where cavities are compressed but inter-tube interaction is maximised, (b) Tilted variant. Infinite bi-layer is not shown.

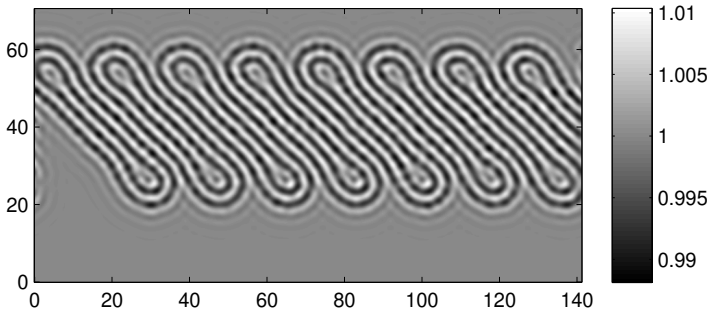

Figure 10: HRTEM simulated images from Density functional theory (DFT) relaxed cross-section for stacked 1D-row of collapsed double-walled BN nanotubes. *there are three pictures normally*

structures. *Do the pleat dimensions correspond between theory and experiment?* The interlayer stacking energy in h-BN is around 50% higher than that of graphite (Figure 11), which provides strong driving force towards ordered stacking and away from amorphous and folded structures. Notably this provides the driving force to reduce as far as possible the tilt angle of the kirigami.

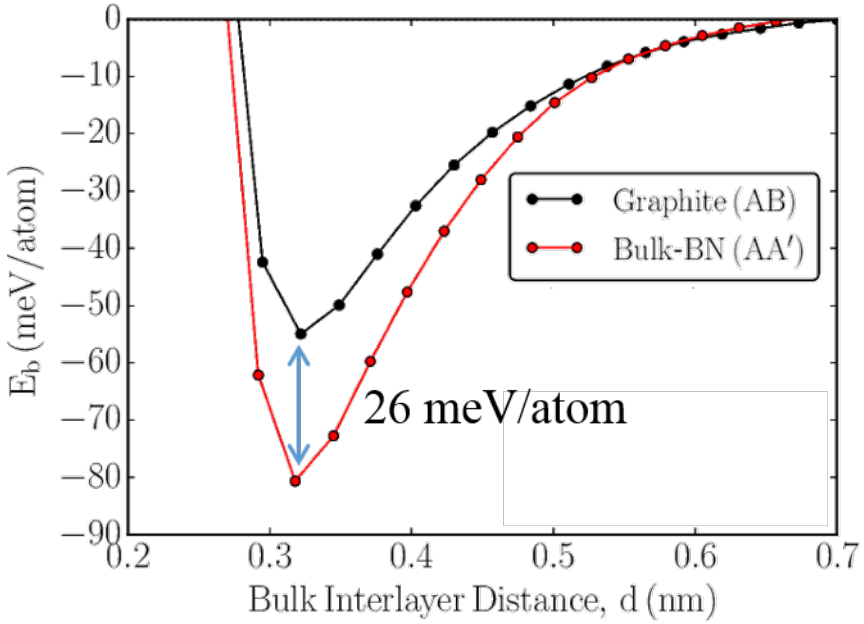

Figure 11: Density functional theory (DFT) calculated interlayer binding enthalpy for Graphite and h-BN using GGA-PBE(D2) theory level as a function of interlayer distance, in most stable stacking configurations.

Pleated kirigami structures confined inside a nanotube under pressure exhibit an interesting structural behaviour: they are able to respond in a uniform analogue way to applied pressure (either axially or from geometric distortion of the external confining tubes) by varying the tilt angle of the pleating, while still maintaining uniform interlayer spacing along the repeat direction. This is not true for a conventional tubular structure where radial compression leads to non-uniform buckling and imposes local variation in interlayer spacing (this is partially compensated in our current systems through facetting). Maintaining uniform interlayer spacing is a strong driving force in hexagonal boron nitride where the ionic interlayer forces are particularly strong, notably compared to graphite. This therefore may be

a driving force for kirigami formation in these MWBNNTs, along with a reason why such structures have not been observed in equivalent MWCCNTs.

We note that our modelling considers only 1D-periodicity and does not introduce the additional experimental complexity of kirigami in two dimensions necessary to fit such structures into a tube. Polygonised kirigami pleats will involve additional mass reorganisation along the polygon facets and are beyond the capabilities of our DFT models at this time.

Discussion

First of all, both our experiments and calculations show the prominence of polygonization in BNNTs at ambient conditions. This constitutes a very important difference with respect to CNTs for which the circular cross-section is the paradigm at ambient conditions. Polygonal structures have been rarely observed[64] in CNTs and most commonly it is reported the tube self-collapse for large tube diameters.[47,65] Our TEM images at ambient pressure (Fig. 1.a1-a2) show the characteristic spotty signature which has been assigned, as already discussed to an helical polygonization of the internal nanotubes. Tube polygonization is in fact also confirmed by our HRTEM tomography images (Fig. 2 and S.I. videos). Our calculations have been only done in very few-walled tubes, but clearly show a tendency for the radial deformation of MWBNNTs including their polygonization at ambient pressures. Such polygonization appears in tubes in a large range of diameters. Only for the largest tube diameters perfectly circular cross-sections were sometimes observed. On the other side, for the smallest tubes, the internal tubes were much more deformed that the exterior ones which in some cases show almost circular cross-sections. We can conclude that both experiments and calculations show tube polygonization in larger tubes with many walls. Calculations also show the presence of pinches in the longitudinal tube direction. In Fig. 1.a3 it is shown a kind of structure observed at ambient conditions showing a non-symmetric local defect which may be assigned to a pinch.

Our TEM study on recovered samples after a pressure cycle shows that boron nitride multi-wall nanotubes tubular structure can be preserved up to pressure cycles of at least 36 GPa (Fig. 1) or even beyond. Nevertheless morphological changes in the tubes can already be observed for tubes cycled up to pressures as low as 7 GPa (Figure 1 b1. to b.4) and confirmed by Raman spectroscopy. Changes include the formation of alveolar structures either with regular bamboo-like morphologies or with irregular alveoli, tube folding or highly damaged tubes including the formation of folded nano-ribbon kirigami internal structures. Preserved tubes with such internal morphologies appear as dominant at the highest pressures, which may be related to a mechanical stabilizing role of the observed internal structures (bamboo-like segmentation or alveoli).

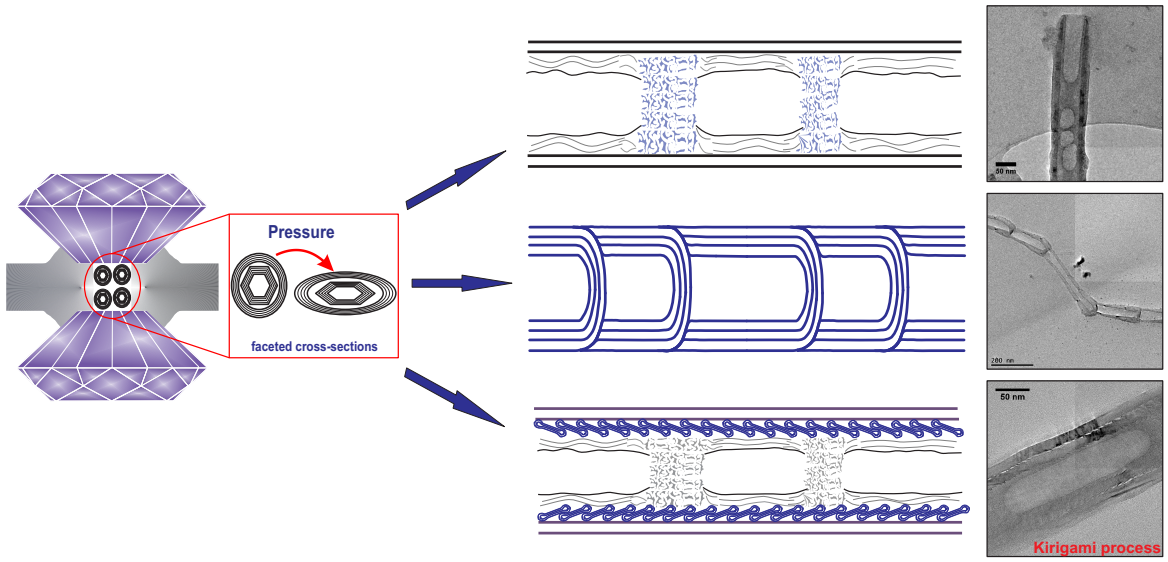

Figure 12: Scheme illustrating the main morphologies for BNNTs after pressure cycle found in this work. On the left side is schematized the diamond anvil cell containing the BNNTs consisting on polygonized inner tubes (not to scale). The zoom pictures pressure induced changes in the nanotubes radial cross-sections. On right side, we have respectively presented the three main BNNTs morphologies identified in our work after pressure cycle. From top to bottom: the alveolar structure, the bamboo-like structure and the kirigami structure (see text for details).

As already discussed, various experimental works indicate the possible evolution of MWBNNTs towards sp^3 forms including w-BN.[51,52] We may then interrogate ourselves about the possibility that the new Raman peak tat we observe at 1280 cm^{-1} in the spectra of samples

cycled from 15.6 GPa and above (Fig. 21.b in S.I.), could be related with such type of transformation. Various theoretical calculations on the active Raman modes of the w-BN structure[66–68] point to a w-BN Raman peak at $\sim$ 1280 cm^{-1} which may then correspond to the new mode observed here. The assignment of that mode is not clear and depending on calculations concordance with A_1(TO) or E_1(LO) symmetries have been proposed. It is important to note that the E_{2g} BNNT mode is preserved in our Raman experiments during compression up to 24 GPa. This observation seems to be consistent with the high resilience of the tube structure.[69,70] Nevertheless, Fig. S2.b clearly shows that non-reversible changes take place on the BNNT structure from pressures above $\sim$ 8 GPa. On the other side, our TEM images show structural modifications of the tubes, but no clear evidence of formation of w-BN.

We have observed a number of structures on MWBNNTs after high pressure cycles which include: i) bamboo-like structures (Fig. 1 b.1, c.2 and d.4), ii) alveolar structures (Fig. 1 b.4 and d.1) iii) hybrid tubular/folded-nanoribbon (Fig. 3) which also presents an alveolar structure. Local densification or radial deformation are also observed in some cases.

Our TEM tomography study (Fig. 2) allows to see that the alveoli correspond to the presence of badly-organized matter inside the tubes. A proposal is that this badly-organized matter could correspond to the breaking of the internal tubes leading to disorganized h-BN ribbon structures. Breaking of the innermost tubes could then lead to self-folding and the particular kirigami-like structure of Fig. 3 or to alveolar structures when no organized self-folding takes place. The presence of alveoli in Fig. 3 would indicate that some internal tube-walls did not self-fold on breaking. In general, the observed alveolar and bamboo-like structures appearing after high pressure treatment show to be quite regular with characteristic longitudinal distances of the order of 100-200 nm. We have observed longitudinal modifications also in the ambient conditions modelling of 3-walled BNNTs (Fig. 6) as well as in the high pressure modelling (Fig. 7). Presently we can not stablish a correlation between the alveolar/bamboo-like structures experimentally observed and the regular longi-

tudinal pinch appearing in the calculations. We may also note that our model points out to a higher reactivity of the pinch regions at high pressures which can be related to the cell-type organization or the bamboo-like one.

We now discuss possible reasons leading to the pressure induced break of internal tubes and not to external ones. We should note that such internal tube breaking mechanism has been never reported in CNTs. Most probably this can be assigned to an additional stress term related to the BNNTs cross-section faceting of internal tubes. This faceting in BNNTs has found to be related to the interlayer lattice registry patterning, which arises from the interlayer electrostatic interactions of BN partly ionic bonds (polar nature).[61] As discussed, our reactive molecular dynamics modelling confirm the tendency for easier faceting in lower diameter systems, which is in good correspondence with the experimental observation of internal tubes faceting.

As already evoked in the introduction, a number of calculations support the idea that radial collapse should take place in BN-nanotubes in the same way as in carbon nanotubes. A simple collapse introduces a symmetry mirror plane along the tube. A n-polygonization with n even can be congruent with that mirror plane, but not if n is odd. The presence of an helical-polygonization will introduce a loss of congruence between the two forms of symmetry (collapse and polygonization) with discrete coincidences along the tube. To further complicate the global picture, we may imagine that in certain circumstances, radial deformation could have a torsional character or that higher order collapse structures can take place.[54] Vertices of the polygons introduce a supplementary local stress which can be reinforced in the collapse mirror plane direction and lead to breaking of the structure during collapse. In a multi-wall structure congruence between the two deformation symmetries would depend on the diameter and could only be eventually obtained for a given small number of tubes, where an organized breaking could take place. We may dress such scenario to explain the hybrid kirigami-alveolar structure observed in Fig. 3. Our DFT modelling shows that the observed internal organized structures can be interpreted in terms of stacked folds.

We can then try to understand the different high pressure MWBNNT observed morphologies as related to the possible schemes of the internal tubes polygonization. Fig.12 summarizes the proposed scheme of pressure transformation. For low polygonal order a symmetric breaking of the internal tubes at pinch locations may lead to the organized folding of the h-BN nanoribbons producing the bamboo-like structures. This would correspond to the case of an even polygon. In the case of an n-polygon with n odd, pressure induced ovalization will not lead to a symmetric stress distribution in the internal tube. A less organized folding of the h-BN nanoribbons would lead to the alveolar structure. The case of the organized stacking of folded h-BN nanoribbons (c) could be related to the multiple fracture of high n-order polygon leading to the kirigami-like structure. In any case the observed structure clearly evidences the existence of a spiral ordering for the internal polygonized tubes.[55,57,61]

Conclusions

Combining the MWBNNTs study with TEM and Raman spectroscopy with MD and DFT modelling of we have found a number of marked structural differences between BNNTs and CNTs. First of all our work confirms the prominence of polygonization in MWBNNTs even at ambient conditions. We have then shown that the high pressure application in MWBNNTs leads to the nanotube transformation into various types of tube morphologies, some of them never observed in CNTs. Some tubular geometries can stand pressures of at least 49 GPa. The observed pressure induced tube morphologies are bamboo-like, disorganized alveolar and kirigami-formed folded boron nitride nanoribbons encapsulated inside a BNNT. These structures can be interpreted as due to different types of arrangement of h-BN nanoribbons formed by the fracture of polygonized internal tubes leading to different types of internal organizations (Fig. 12). The formation of such internal structures appears to favour then the mechanical stability of the nanotubular geometry.

The overall high pressure evolution of MWBNNTs appears then as being very different from the one of carbon nanotubes. In particular the formation of modulates structures along the tube axis (polygonization or alveolar structuration) differs from the usual radial collapse mechanism in carbon nanotubes for which no axial structural components have been proposed. The physical properties of these new tubular morphologies needs further study and may provide new paths to explore opportunities in the design of novel mechanical reinforced materials or electro-optical tuned devices.

Experimental Section

Sample synthesis: High quality BNNTs were synthesized via Boron Oxide Chemical Vapor Deposition (BOCVD) following a catalytic "Vapour-Liquid-Solid (VLS) Growth Mechanism".[71–73] A mixture of powder precursors (boron B) and catalysts (magnesium oxide MgO and iron boride FeB) in a molar ratio of $1:2:1$ respectively, was used as a starting material. This mixture was put in an alumina combustion boat and placed in a horizontal induction tube furnace closed at both ends. The tube furnace was first evacuated and then heated up to 1500 °C. As a result, B_2O_2 vapours and liquid or partially-melted nanosize catalyst particles were formed. NH_3 gas was then introduced into the tube furnace at a rate of 150 sccm for one hour at a pressure of 1000 mbar. At this temperature NH_3 decomposed into N_2 and H_2. The oxygen of the as-formed B_2O_2 vapours reacted with H_2 to form water vapours while the boron reacted with N_2 to form BN-species. These species were then diffused into the condensed catalysts and aggregated with time until it supersaturated and precipitated into the form of BNNTs. BNNTs thus obtained were multiwall nanotubes (MWNTs) in pure form, with an average outer diameter of approximately 50 nm, a length of greater than 10 mm with almost no impurity present in the final product. The nanotubes were straight with concentric tubular structure containing no defects and were uniformly dispersed (see later figure with TEM images).

High Pressure Raman Spectroscopy: The BN-nanotubes were studied at high-pressure using *in situ* Raman spectroscopy with a membrane diamond-anvil cell (DAC) having diamond culets of 350 μm. The MWBNNTs samples were inserted in a 120 μm diameter hole drilled in a pre-idented stainless steel gasket (thickness after identation $\sim$ 30 μm). A small ruby chip placed in the sample chamber was used as the *in situ* pressure gauge with the use of the ruby fluorescence method .[74] NaCl was used as pressure-transmitting medium (PTM). Raman spectra were collected in backscattering geometry with a home-built optical system and an Acton SpectraPro 2500i spectrometer with an spectral resolution of $\sim$2 cm^{-1}. The excitation energy was 2.41 eV (514.5 nm) provided by an air-cooled argon-ion laser, having a source power limited to 20 mW to avoid heating sample effects (see Figure S1 of the Supporting Information, no significant changes related to the displacement of the tangential BNMWNT mode is observed, only parameters such as spectral profiles, background and signal-to-noise ratio showed variations between spectra). A Mitutoyo 50x objective lens allowed to focus the laser beam to a spot size of 2 μm at the sample. Three *in situ* Raman experiments were performed up to maximum pressures of 7.1, 15.6 and 36 GPa. The Raman spectra of the experiments up to pressures of 41.1 GPa and 48.6 GPa were measured only after pressure release (out of the DAC). For these spectra we used a LabRAM HR Evolution spectrometer (with a spectral resolution of $\sim$ 0.5 cm^{-1}) with a excitation laser energy of 2.33 eV. The laser beam was focused onto the samples using a long work distance 50x Mitutoyo magnification objective lens. In all experiments samples were recovered after the pressure cycle for further characterizations.

Characterization via electron microscopy: TEM observations of the *as-produced* BN-NTs as well as the pressure cycled samples were performed on a 200 keV field-emission high-resolution transmission electron microscope (TEM) JEOL JEM-2100F. From the TEM images the inner diameter of the synthesized MWBNNTs ranges from 15 to 20 nm and the outer tube diameter from 40 to 80 nm. Some larger tubes can be also observed exceptionally.

TEM tomography series of tilted images were also taken for the pristine BN-nanotubes

sample and for the cycled sample up to 36 GPa samples. For this, the JEOL JEM-2100F TEM was equipped with a Gatan Ultrascan 1000 CCD camera, using a magnification of 40000 for the pristine samples and of 80000 for the 36 GPa cycled sample. The specimens were rotated from $-60°$ to $66°$ in case of the pristine BN-nanotube and from $-60°$ to $63°$ for the recovered BN-nanotube. A Saxton tilt increment scheme (variable angular step allowing to improve 3D reconstruction with a reduced number of images in order to preserve the beam sensitive structure of the sample) was used. For the acquisitions control and 3D reconstructions, a JEOL TEMography software package was used. 3D visualization of the reconstructed structures were performed with ImageJ software .[75]

Supporting Information

Supporting Information is available from the Wiley Online Library or from the author:

- Laser heating effect on BNNTs samples, Electron tomography videos of MWBNNT pristine and MWBNNT after 36 GPa pressure cycle, Raman spectroscopy results of MWBNNTs at high pressures, Modelling methodology.

ORCID

S.D. Silva-Santos: 0000-0002-0557-2492

Notes

The authors declare no competing financial interest.

Acknowledgements

This work has been done thanks to the support of the PLECE, CECOMO and CTμ platforms of the University of Lyon. SDSS acknowledges the support from the "Science Without

Borders" program of the CNPq/Brazil (grant 248850/2013-0). We thank also the French-Brazilian CAPES-COFECUB program through project Ph 938/19. A.S-M., CJ and BT acknowledge support from the iMUST LABEX program MUSCAT-2D. J.M.S., and A.L.A. thank the Laboratório de Simulação Computacional Cajuína (LSCC) at Universidade Federal do Piauí for computational support. A.L.A acknowledges CENAPAD-SP for computer time and the Brazilian agencies CNPq (Processes no. 427175/2016-0 and 313845/2018-2) for financial support. J.M.S. thanks CAPES, CNPq, FAPESP and the Center for Computational Engineering and Sciences at Unicamp for computational support through the FAPESP/CEPID Grant 2013/08293-7.

References

(1) Xu, S.; Yan, Z.; Jang, K.-I.; Huang, W.; Fu, H.; Kim, J.; Wei, Z.; Flavin, M.; McCracken, J.; Wang, R.; Badea, A.; Liu, Y.; Xiao, D.; Zhou, G.; Lee, J.; Chung, H. U.; Cheng, H.; Ren, W.; Banks, A.; Li, X.; Paik, U.; Nuzzo, R. G.; Huang, Y.; Zhang, Y.; Rogers, J. A. *Science* **2015**, *347*, 154–159.

(2) Shenoy, V. B.; Gracias, D. H. *MRS Bulletin* **2012**, *37*, 847–854.

(3) Zhang, Y.; Yan, Z.; Nan, K.; Xiao, D.; Liu, Y.; Luan, H.; Fu, H.; Wang, X.; Yang, Q.; Wang, J.; Ren, W.; Si, H.; Liu, F.; Yang, L.; Li, H.; Wang, J.; Guo, X.; Luo, H.; Wang, L.; Huang, Y.; Rogers, J. A. *Proceedings of the National Academy of Sciences* **2015**, *112*, 11757–11764.

(4) Yan, Z.; Zhang, F.; Liu, F.; Han, M.; Ou, D.; Liu, Y.; Lin, Q.; Guo, X.; Fu, H.; Xie, Z.; Gao, M.; Huang, Y.; Kim, J.; Qiu, Y.; Nan, K.; Kim, J.; Gutruf, P.; Luo, H.; Zhao, A.; Hwang, K.-C.; Huang, Y.; Zhang, Y.; Rogers, J. A. *Science Advances* **2016**, *2*, e1601014.

(5) Kim, K.; Lee, Z.; Malone, B. D.; Chan, K. T.; Alemán, B.; Regan, W.; Gannett, W.; Crommie, M. F.; Cohen, M. L.; Zettl, A. *Phys. Rev. B* **2011**, *83*, 245433.

(6) Song, Q.; An, M.; Chen, X.; Peng, Z.; Zang, J.; Yang, N. *Nanoscale* **2016**, *8*, 14943–14949.

(7) Cao, C.; Feng, Y.; Zang, J.; López, G. P.; Zhao, X. *Extreme Mechanics Letters* **2015**, *4*, 18 – 25.

(8) Bolaños Quiñones, V. A.; Zhu, H.; Solovev, A. A.; Mei, Y.; Gracias, D. H. *Advanced Biosystems* **2018**, *2*, 1800230.

(9) Machon, D.; Pischedda, V.; Le Floch, S.; San-Miguel, A. *Journal of Applied Physics* **2018**, *124*, 160902.

(10) Bousige, C.; Balima, F.; Machon, D.; Pinheiro, G. S.; Torres-Dias, A.; Nicolle, J.; Kalita, D.; Bendiab, N.; Marty, L.; Bouchiat, V.; Montagnac, G.; Souza Filho, A. G.; Poncharal, P.; San-Miguel, A. *Nano Letters* **2017**, *17*, 21–27.

(11) Machon, D.; Bousige, C.; Alencar, R.; Torres-Dias, A.; Balima, F.; Nicolle, J.; de Sousa Pinheiro, G.; Souza Filho, A. G.; San-Miguel, A. *Journal of Raman Spectroscopy* **2018**, *49*, 121–129.

(12) Alencar, R. S.; Saboia, K. D. A.; Machon, D.; Montagnac, G.; Meunier, V.; Ferreira, O. P.; San-Miguel, A.; Souza Filho, A. G. *Phys. Rev. Materials* **2017**, *1*, 024002.

(13) Elliott, J. A.; Sandler, J. K. W.; Windle, A. H.; Young, R. J.; Shaffer, M. S. P. *Phys. Rev. Lett.* **2004**, *92*, 095501.

(14) Xiao, J.; Liu, B.; Huang, Y.; Zuo, J.; Hwang, K.-C.; Yu, M.-F. *Nanotechnology* **2007**, *18*, 395703.

(15) Cerqueira, T. F.; Botti, S.; San-Miguel, A.; Marques, M. A. *Carbon* **2014**, *69*, 355–360.

(16) Loa, I. *Journal of Raman Spectroscopy* **2003**, *34*, 611–627.

(17) Caillier, C.; Machon, D.; San-Miguel, A.; Arenal, R.; Montagnac, G.; Cardon, H.; Kalbac, M.; Zukalova, M.; Kavan, L. *Phys. Rev. B* **2008**, *77*, 125418.

(18) Yao, M.; Wang, Z.; Liu, B.; Zou, Y.; Yu, S.; Lin, W.; Hou, Y.; Pan, S.; Jin, M.; Zou, B.; Cui, T.; Zou, G.; Sundqvist, B. *Phys. Rev. B* **2008**, *78*, 205411.

(19) Aguiar, A. L.; Barros, E. B.; Capaz, R. B.; Souza Filho, A. G.; Freire, P. T. C.; Mendes Filho, J.; Machon, D.; Caillier, C.; Kim, Y. A.; Muramatsu, H.; Endo, M.; San-Miguel, A. *J. Phys. Chem. C* **2011**, *115*, 5378–5384.

(20) Alencar, R. S.; Aguiar, A. L.; Paschoal, A. R.; Freire, P. T. C.; Kim, Y. A.; Muramatsu, H.; Endo, M.; Terrones, H.; Terrones, M.; San-Miguel, A.; Dresselhaus, M. S.; Souza Filho, A. G. *Journal of Physical Chemistry C* **2014**, *118*, 8153–8158.

(21) Torres-Dias, A. C.; Cerqueira, T. F.; Cui, W.; Marques, M. A.; Botti, S.; Machon, D.; Hartmann, M. A.; Sun, Y.; Dunstan, D. J.; San-Miguel, A. *Carbon* **2017**, *123*, 145 – 150.

(22) Mases, M.; Milyavskiy, V. V.; Waldbock, J.; Dossot, M.; Devaux, X.; McRae, E.; Soldatov, A. V. *physica status solidi (b)* **2012**, *249*, 2378–2381.

(23) Silva Santos, S.; Silva Alencar, R.; Aguiar, A.; Kim, Y.; Muramatsu, H.; Endo, M.; Blanchard, N.; San-Miguel, A.; Filho, A. *Carbon* **2019**, *141*, 568–579.

(24) Coutinho, S. S.; Lemos, V.; Guerini, S. *Phys. Rev. B* **2009**, *80*, 193408.

(25) Kinoshita, Y.; Hase, S.; Ohno, N. *Phys. Rev. B* **2009**, *80*, 125114.

(26) Melo, W. S.; Pereira, M. B.; Silva Filho, H. F.; Guerini, S. *The European Physical Journal B* **2015**, *88*, 6.

(27) Liao, Y.; Chen, Z.; Connell, J. W.; Fay, C. C.; Park, C.; Kim, J.-W.; Lin, Y. *Advanced Functional Materials* **2014**, *24*, 4497–4506.

(28) Kim, D.; Muramatsu, H.; Kim, Y. A. *Nanoscale Research Letters* **2017**, *12*, 94.

(29) Rubio, A.; Corkill, J.; Cohen, M. *Phys. Rev. B* **1994**, *49*, 5081–5084.

(30) Blase, X.; Rubio, A.; Louie, S.; Cohen, M. *EPL (Europhysics Letters)* **1994**, *28*, 335–340.

(31) Chopra, N. G.; Luyken, R. J.; Cherrey, K.; Crespi, V. H.; Cohen, M. L.; Louie, S. G.; Zettl, A. *Science* **1995**, *269*, 966–967.

(32) Han, W.-Q.; Yu, H.-G.; Zhi, C.; Wang, J.; Liu, Z.; Sekiguchi, T.; Bando, Y. *Nano Letters* **2008**, *8*, 491–494.

(33) Lee, C. H.; Xie, M.; Kayastha, V.; Wang, J.; Yap, Y. K. *Chemistry of Materials* **2010**, *22*, 1782–1787.

(34) Golberg, D.; Bando, Y.; Kurashima, K.; Sato, T. *Scripta Materialia* **2001**, *44*, 1561 – 1565.

(35) Chen, Y.; Zou, J.; Campbell, S. J.; Le Caer, G. *Applied Physics Letters* **2004**, *84*, 2430–2432.

(36) Xiao, Y.; Yan, X. H.; Cao, J. X.; Ding, J. W.; Mao, Y. L.; Xiang, J. *Phys. Rev. B* **2004**, *69*, 205415.

(37) Verma, V.; Jindal, V. K.; Dharamvir, K. *Nanotechnology* **2007**, *18*, 435711.

(38) Golberg, D.; Bando, Y.; Huang, Y.; Terao, T.; Mitome, M.; Tang, C.; Zhi, C. *ACS Nano* **2010**, *4*, 2979–2993.

(39) Zhi, C.; Bando, Y.; Tang, C.; Golberg, D. *Materials Science and Engineering: R: Reports* **2010**, *70*, 92 – 111.

(40) Ciofani, G. *Expert Opinion on Drug Delivery* **2010**, *7*, 889–893.

(41) Ciofani, G.; Raffa, V.; Menciassi, A.; Dario, P. *Journal of Nanoscience and Nanotechnology* **2008**, *8*, 6223–6231.

(42) Danti, S.; Ciofani, G.; Pertici, G.; Moscato, S.; D'Alessandro, D.; Ciabatti, E.; Chiellini, F.; D'Acunto, M.; Mattoli, V.; Berrettini, S. *Journal of Tissue Engineering and Regenerative Medicine* **2015**, *9*, 847–851.

(43) Coleman, J. N.; Khan, U.; Blau, W. J.; Gun'ko, Y. K. *Carbon* **2006**, *44*, 1624 – 1652.

(44) Zheng, M.; Chen, X.; Bae, I.-T.; Ke, C.; Park, C.; Smith, M. W.; Jordan, K. *Small* **2012**, *8*, 116–121.

(45) Zheng, M.; Ke, C.; Bae, I.-T.; Park, C.; Smith, M. W.; Jordan, K. *Nanotechnology* **2012**, *23*, 095703.

(46) Torres-Dias, A. C.; Cambré, S.; Wenseleers, W.; Machon, D.; San-Miguel, A. *Carbon* **2015**, *95*, 442 – 451.

(47) Magnin, Y.; Rondepierre, F.; Cui, W.; Dunstan, D. J.; San-Miguel, A. Carbon nanotubes collapse phase diagram with arbitrary number of walls. Collapse modes and macroscopic analog. 2021.

(48) You, S.; Mases, M.; Dobryden, I.; Green, A. A.; Hersam, M. C.; Soldatov, A. V. *High Pressure Res.* **2011**, *31*, 186–190.

(49) Saha, S.; Muthu, D.; Golberg, D.; Tang, C.; Zhi, C.; Bando, Y.; Sood, A. *Chemical Physics Letters* **2006**, *421*, 86 – 90.

(50) Saha, S.; Gadagkar, V.; Maiti, P. K.; Muthu, D. V. S.; Golberg, D.; Tang, C.; Zhi, C.; Bando, Y.; Sood, A. K. *Journal of Nanoscience and Nanotechnology* **2007**, *7*, 1810–1814.

(51) Muthu, D.; Midgley, A.; Petruska, E.; Sood, A.; Bando, Y.; Golberg, D.; Kruger, M. *Chemical Physics Letters* **2008**, *466*, 205–208.

(52) Dong, Z.; Song, Y. *The Journal of Physical Chemistry C* **2010**, *114*, 1782–1788.

(53) Meng, Y.; Mao, H.-K.; Eng, P. J.; Trainor, T. P.; Newville, M.; Hu, M. Y.; Kao, C.; Shu, J.; Hausermann, D.; Hemley, R. J. *Nat Mater* **2004**, *3*, 111–114.

(54) Balima, F.; Floch, S. L.; Adessi, C.; Cerqueira, T. F.; Blanchard, N.; Arenal, R.; Brûlet, A.; Marques, M. A.; Botti, S.; San-Miguel, A. *Carbon* **2016**, *106*, 64–73.

(55) Celik-Aktas, A.; Zuo, J.-M.; Stubbins, J. F.; Tang, C.; Bando, Y. *Acta Crystallographica Section A* **2005**, *61*, 533–541.

(56) Pierret, A.; Nong, H.; Fossard, F.; Attal-Trétout, B.; Xue, Y.; Golberg, D.; Barjon, J.; Loiseau, A. *Journal of Applied Physics* **2015**, *118*, 234307.

(57) Golberg, D.; Mitome, M.; Bando, Y.; Tang, C.; Zhi, C. *Applied Physics A* **2007**, *88*, 347–352.

(58) Xu, X. G.; Gilburd, L.; Bando, Y.; Golberg, D.; Walker, G. C. *The Journal of Physical Chemistry C* **2016**, *120*, 1945–1951.

(59) Aurélie, P. Propriétés structurales et optiques de nanostructures III-N semiconductrices à grand gap: Nanofils d'$Al_xGa_{1-x}N$ synthétisés par épitaxie par jets moléculaires et nanostructures de nitrure de bore. Ph.D. thesis, Université Pierre et Marie Curie, 2013.

(60) Golberg, D.; Costa, P. M. F. J.; Lourie, O.; Mitome, M.; Bai, X.; Kurashima, K.; Zhi, C.; Tang, C.; Bando, Y. *Nano Letters* **2007**, *7*, 2146–2151.

(61) Leven, I.; Guerra, R.; Vanossi, A.; Tosatti, E.; Hod, O. *Nat Nano* **2016**, *11*, 1082–1086.

(62) Prawer, S.; Nemanich, R. J. *Philosophical Transactions of the Royal Society of London A: Mathematical, Physical and Engineering Sciences* **2004**, *362*, 2537–2565.

(63) Aguiar, A. L.; Capaz, R. B.; Souza Filho, A. G.; San-Miguel, A. *The Journal of Physical Chemistry C* **2012**, *116*, 22637–22645.

(64) Zhang, X. F.; Zhang, Z. *Phys. Rev. B* **1995**, *52*, 5313–5317.

(65) Zhang, C.; Bets, K.; Lee, S. S.; Sun, Z.; Mirri, F.; Colvin, V. L.; Yakobson, B. I.; Tour, J. M.; Hauge, R. H. *ACS Nano* **2012**, *6*, 6023–6032.

(66) Karch, K.; Bechstedt, F. *Phys. Rev. B* **1997**, *56*, 7404–7415.

(67) Ohba, N.; Miwa, K.; Nagasako, N.; Fukumoto, A. *Phys. Rev. B* **2001**, *63*, 115207.

(68) Cai, Y.; Zhang, L.; Zeng, Q.; Cheng, L.; Xu, Y. *Solid State Communications* **2007**, *141*, 262 – 266.

(69) Garel, J.; Leven, I.; Zhi, C.; Nagapriya, K. S.; Popovitz-Biro, R.; Golberg, D.; Bando, Y.; Hod, O.; Joselevich, E. *Nano Letters* **2012**, *12*, 6347–6352.

(70) Wei, X.; Wang, M.-S.; Bando, Y.; Golberg, D. *Advanced Materials* **2010**, *22*, 4895–4899.

(71) Tang, C.; Bando, Y.; Sato, T.; Kurashima, K. *Chem. Commun.* **2002**, 1290–1291.

(72) Zhi, C.; Bando, Y.; Tan, C.; Golberg, D. *Solid State Communications* **2005**, *135*, 67 – 70.

(73) Huang, Y.; Lin, J.; Tang, C.; Bando, Y.; Zhi, C.; Zhai, T.; Dierre, B.; Sekiguchi, T.; Golberg, D. *Nanotechnology* **2011**, *22*, 145602.

(74) Mao, H. K.; Xu, J.; Bell, P. M. *Journal of Geophysical Research: Solid Earth* **1986**, *91*, 4673–4676.

(75) Schneider, C. A.; Rasband, W. S.; Eliceiri, K. W. *Nature Methods* **2012**, *9*, 671–675.

Graphical TOC Entry

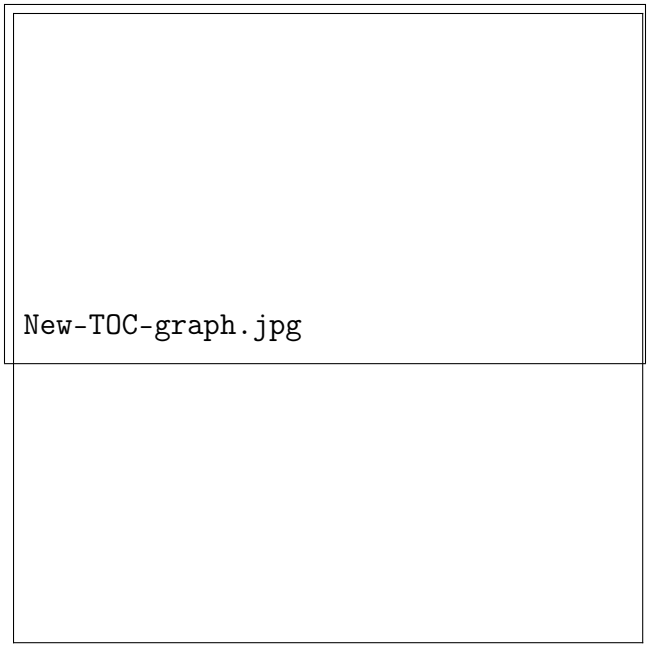

High pressure tailoring in boron nitride nanotubes to generate folded h-BN nanoribbons - *kirigami*.